Improving Cloud-Top Divergence Signals with a Bilateral Filter

Jackson C. Tobin

Cooperative Institute for Research in the Atmosphere, Colorado State University, Fort Collins, Colorado.

Abstract

Severe weather intensity trends can be monitored from satellite imagery over regions with sparse radar coverage using novel products available from optical flow retrievals. For example, cloud-top divergence rendered from the retrieved brightness motions, provides an indirect measure of updraft intensity with time. Recent demonstrations have now shown that dense optical flow can render sub-storm scale (< 5 km) motions, which appear noisy to operational forecasters during warning operations evaluations. The bilateral filter, a spatial signal smoothing filter that retains large-scale features while attenuating signal noise, is an approach for removing any unwanted cloud-top divergence noise signals while preserving the large-scale signals forecasters use in practice. Little is currently understood, however, on how such filters modify observed trends and magnitudes in cloud-top divergence, in particular how such magnitudes change during and in advance of severe weather observations at the ground. Two bilateral filter sizes were evaluated on a mid-latitude supercell in the Great Plains and tropical convection off the Northeast coast of South America, and it was determined that a bilateral filter with a gaussian sigma size of 2.5 adequately removed unwanted signals for both cases while maintaining the 5 min severe weather lead time associated with cloud-top divergence. Additionally, filtered signals were reduced by ~38% to ~60% for sigma sizes of 2.5 and 5.0 respectively.

Section 1. Introduction

Severe weather conditions characterized by powerful winds, tornadoes, and hail, inflict substantial damage upon communities throughout the United States annually. In 2024 alone, severe weather cost 51 United States citizens lives and $41.3B in damages (U.S. Billion-Dollar Weather Disasters, 2025). Meteorologists typically observe these features via ground-based dual-polarization radar. Unfortunately, radar has limited spatial coverage over the United States – particularly in unpopulated regions, mountainous regions, and bodies of water, and limited temporal coverage, often with updates only provided every ~5 min. The introduction of Geostationary (GEO) Operational Environmental Satellites (GOES) provides fine spatial (down

to 0.5 km), spectral (2 visible and 4 near infrared and 10 infrared band), and temporal resolution (≤1min) imagery over observed storms with near-hemispheric coverage w.

The Super Rapid Scan (SRS) capabilities of GOES-R enable retrievals of Optical Flow (OF) fields for most cloud-drift motions. New OF retrieval methods can even render dense (every image pixel) motions which allow for the resolution of fine-scale flow fields and subsequent properties. OF enables a variety of new products in satellite imagery like the retrieval of atmospheric winds (Velden et al. 2005), improvements in multi-satellite image compositing via temporal interpolation (*in review* Apke et al. 2024), simulated mesosectors over the Continental United States (CONUS) (Rogers, et al. 2020), and feature tracking relevant for atmospheric sciences such as inferring the presence of outflow boundaries (Apke et al. 2020). Beyond satellite applications, OF is used in autonomous "self-driving" cars, object tracking in advanced security cameras (crowd safety) and traffic monitoring systems (traffic diagnostics and speed regulation), and special effects for computer-generated imagery (CGI) in movies like *Avatar* (2009) and *The Matrix* (1999; Fortune et al. 2015).

This paper focuses on OF for satellite imagery in Cloud-Top Divergence (CTD) derivation. CTD is a measure of outflow atop a storm via navigated OF fields which can be observed during the mature phase of deep convection (DC). CTD can be linked to tendencies in updrafts via mass continuity at the equilibrium level (i.e. stronger vertical deceleration equates to stronger horizontal outflow which can be detected by the satellite). Previous studies have shown a strong relationship between the intensity of DC and retrieved CTD, including the occurrence of strong downburst winds, tornadogenesis, and large hail growth (Apke 2018 – all sources). Older techniques for retrieving CTD, however, relied on objective analysis from sparse OF retrieval techniques that often missed or mischaracterized flow trends (Apke and Mecikalski 2021). With more novel techniques to render OF now becoming operational, including those which can handle motion discontinuities and strong deformations, it is time to revisit CTD computation, appropriate methods for displaying such data, and typical magnitudes for intense storms.

One main purpose of this paper is to increase the user-interpretability of products using CTD. Feedback from the 2024 HWT highlighted the spatiotemporal noise in CTD signals. Any improvements to CTD signals must be re-evaluated in terms of their lead times, as well as the need for reliable severe weather threshold values for these signals.

The magnitudes of such CTD vary with different retrieval algorithms as the assumptions within OF retrievals and finite differencing of navigated motions vary (i.e. Apke and Mecikalski 2021) Previous methods for OF retrievals (e.g. Apke et al. 2016; 2018) typically resolved flow features on the order of ~20 km, while new OF retrieval methods resolve sub-storm-scale features (~5 km) . Feedback from the 2024 Hazardous Weather Testbed (Theil 2024) included critiques of CTD in such features as noisy "spiderwebbing" (Figure 3) which visually diminished salient CTD signals related to DC intensity. Application of spatial smoothing filters may resolve such artifacts.

This paper evaluates the application of a bilateral filter on the OF motion-fields used for CTD derivation to remove the unwanted CTD signals while maintaining CTD signals related to severe weather, such as large hail (>1in), strong winds, and tornados. This will be crosschecked with Multi-Radar Multi-Sensor (MRMS; Zhang 2016) reflectivity and Maximum Expected Size of Hail (MESH) estimates along with storm reports. Threshold values for various bilateral filter sizes will be derived from MRMS MESH ≥ 1in. Analysis of the case studies will result in CTD threshold value ranges that correspond to severe weather.

Section 2. Background

Optical Flow

OF methods are described in detail in Baker et al. (2011), though a high-level description is provided here. OF is defined as the "distribution of apparent velocities of movement of brightness patterns in an image" (Horn and Schunck 1981). Objective retrieval relies on assumptions that the brightness (and brightness gradients) is unchanging between the two images (as human vision perceives such motions) and are realistically smooth. Methods for retrieval include so-called "Variational" (penalty function minimization) techniques (as in Horn and Schunck 1981), and, more recently, fully data-driven machine-learning based methods (e.g. Teed and Deng 2020). When performed on satellite imagery, such displacements often represent cloud drift motions which can be navigated and height assigned as an approximation for winds (e.g. Velden et al. 2005), used to track features with time (Apke et al. 2020), and even to retrieve time-trends atop moving clouds (e.g. cloud-top cooling; Mecikalski et al. 2006).

An emerging approach for rendering satellite-based cloud-drift motions is the Optical flow Code for Accurate Nowcasting Experiments (OCTANE), first implemented in Apke et al. (2022). OCTANE employs a "Variational" approach by Zimmer et al. (2011) method for retrieving DOF

fields by constructing a global energy functional, following the Brox et. al. (2004) method to minimize this functional. OCTANE outperformed state-of-the-art techniques used for winds retrieval in operations (including what was used in Apke et al. 2018) when compared to a lidar wind-profiler truth dataset and has demonstrated value in retrieving divergence signals relevant to convection intensity and warning operations decision making (Thiel 2023, 2024). While data-driven methods can also derive similar dense optical flows (often with improved overall accuracy), they often suffer from setbacks in retrieving fine-scale motions that are most relevant for meteorological applications (e.g. Hilburn et al. 2020). Hence, this research focuses on using variational retrievals instead to render cloud-top divergence.

Cloud-Top Divergence in Relation to Severe Weather

Apke et al. (2018) noted that "maximum single-Doppler radar-derived radial divergence to infer the strength of observed updrafts and found positive correlations to ground-reported hail diameter." Schultz et al. (2009, 2011) found that these strong updrafts precede severe storm features such as winds, hail, and tornadoes, by nearly 20 minutes (in their case, quantified by changes in observed lightning flashes). Apke et al. (2018) positively correlated SRS mesoscale OF motion fields from the GOES-14 satellite imager to strong horizontal CTD values with upper-level updrafts, objectively identified OTs, and lightning flash rates. These results demonstrate that, regardless of a complex relationship, CTD is linked to and precedes key markers of severe weather.

The derivation of CTD includes a few key assumptions: In Apke et al. (2016, 2018), optical flow motions deemed above a specific altitude (10 km) were inferred to be at a consistent height such that spatial finite differencing could be performed. Furthermore, all motions were assumed to be related to the wind, and not propagation (versus features such as gravity waves which OF retrieval algorithms may detect). Assumptions can break down in the case of features such as Above-Anvil Cirrus Plumes (Bedka et al. 2018) – which can be difficult to objectively identify via satellite – and thin high altitude cirrus which must be reconciled in near real-time products (Apke and Mecikalski 2021). When evaluated directly at the 2024 HWT, several forecasters noted CTD highlighted critical storms with as much as ~15 min lead time, working particularly well in regions absent of radar coverage (Thiel 2024). However, forecasters noted desires to see more information regarding critical magnitudes of cloud-top divergence in advance of severe weather, and for products which rendered divergence of larger spatial scale flows, which will be addressed in the sections to follow.

Section 3. Data & Methods

GOES-16 Data and Mesosectors

All OF and analysis was performed within GOES-16 Advanced Baseline Imager (ABI) Mesosectors, using the Channel 2 0.64µm visible (VIS) "red" band (Schmit et al. 2013). GOES-16 VIS has 0.5km pixel resolution at nadir (sub-satellite point) and is ideal for resolution within mesoscale sectors but is only available during daytime. Conversely, the IR band has 2km pixel resolution at nadir but is available at all times of the day. 1-min temporal resolution GOES-16 Mesosectors allow for DOF retrieval but are only located in two small ~1000 x 1000 km spatial domains. Mesosectors are often centered over high-impact events in the Contiguous United States, but can also be placed over other regions of the Earth Figure 1. Mesosector data is readily available over CONUS, but sparse over tropical regions and South America.

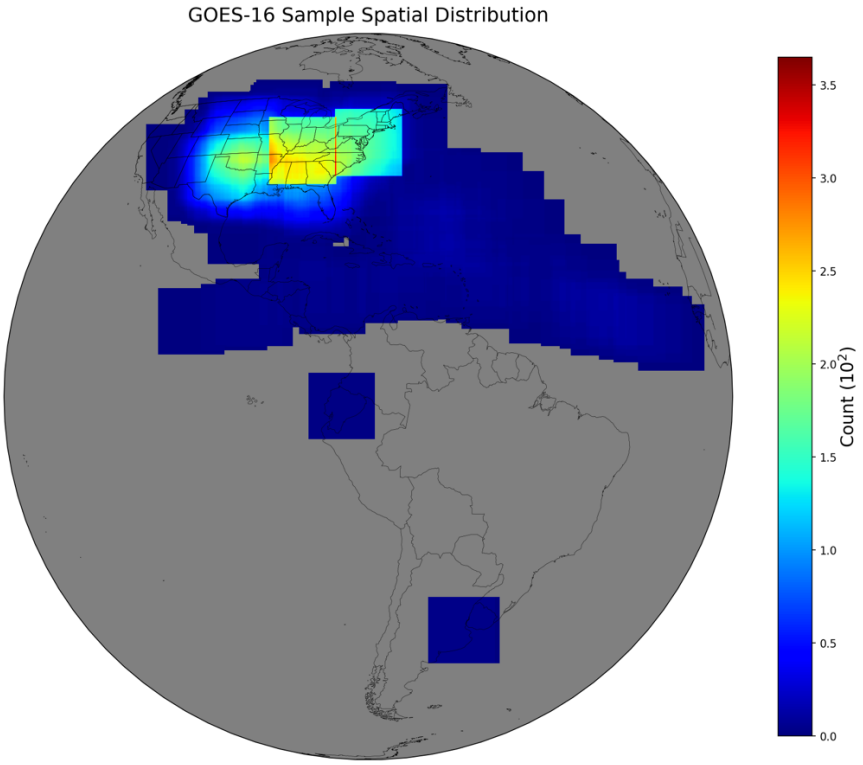

Figure 1: Frequency plot of mesosector locations during the year 2023. The two default locations are centered over the American Midwest and New England.

Parameterization of Optical Flow for GOES-16 Visible Imagery

Computing OF from OCTANE and subsequent CTD derivations requires both the GOES-16 ABI VIS band and the "clean" IR longwave window band. OF retrievals for CTD over deep

convection require 1-min temporal resolution mesosectors to adequately capture motions in regions with rapid condensation, evaporation, and evolution. Scan interval times much greater than 1 minute can result in significant error as assumptions such as brightness constancy break down in the optical flow retrieval.

The *u*- and *v*- motion fields were calculated by OCTANE using VIS 1-min imagery for its fine spatiotemporal resolution. A more detailed derivation of OF and pyramiding methods using OCTANE is outlined in Apke et al. (2022) and in the Appendix. The method used in Apke et al. (2022) is a Zimmer et al. (2011) approach, which defines the global energy functional in terms of 1) the Brox et al. (2004) energy functional which is robust to changes in illumination and motion discontinuities, and 2) a smoothening term. The latter two were tuned via the gradient constancy constraint, λ, and the smoothness constraint, α. The selection for the constraints was based on true winds from ancillary wind lidar information following Apke et al. (2022), where $\lambda = 1$ and $\alpha = 5$, with reflectance factor normalized to floating point values between 0 and 255. After computing *u* and *v* motion fields, they were navigated to the GOES-16 grid using the speed and direction, represented as the velocity vector, $\mathbf{v}$. These motion fields were then passed through the bilateral filter before being used to compute CTD, or $\nabla \cdot \mathbf{v}'$.

Application of the Bilateral Filter

The bilateral filter used in this study consists of a Gaussian spatial-weighting kernel and a Gaussian brightness-weighting kernel (see Appendix). The nonlinearity of the bilateral filter restricts it from a quantitative analysis in the form of a signal response function (SRF), but the spatial Gaussian can be represented in this way. After the motion-fields were navigated to the GOES field and converted to kilometers using, a Fast Fourier Transform (FFT) was performed on the image and the vector magnitude of the motion-fields ($\sqrt{\{\boldsymbol{x} + \boldsymbol{y}\}^2} = r$) were used to relate the spatial frequencies to feature size in meters after a reverse FFT. The SRF is shown in Figure 2 with varying σ. Larger σ sizes result in attenuation of smaller feature sizes. From this analysis alone, σ sizes of 2.5 and 5.0 were picked for further analysis with the bilateral filter due to their resolution of relevant storm-scale features.

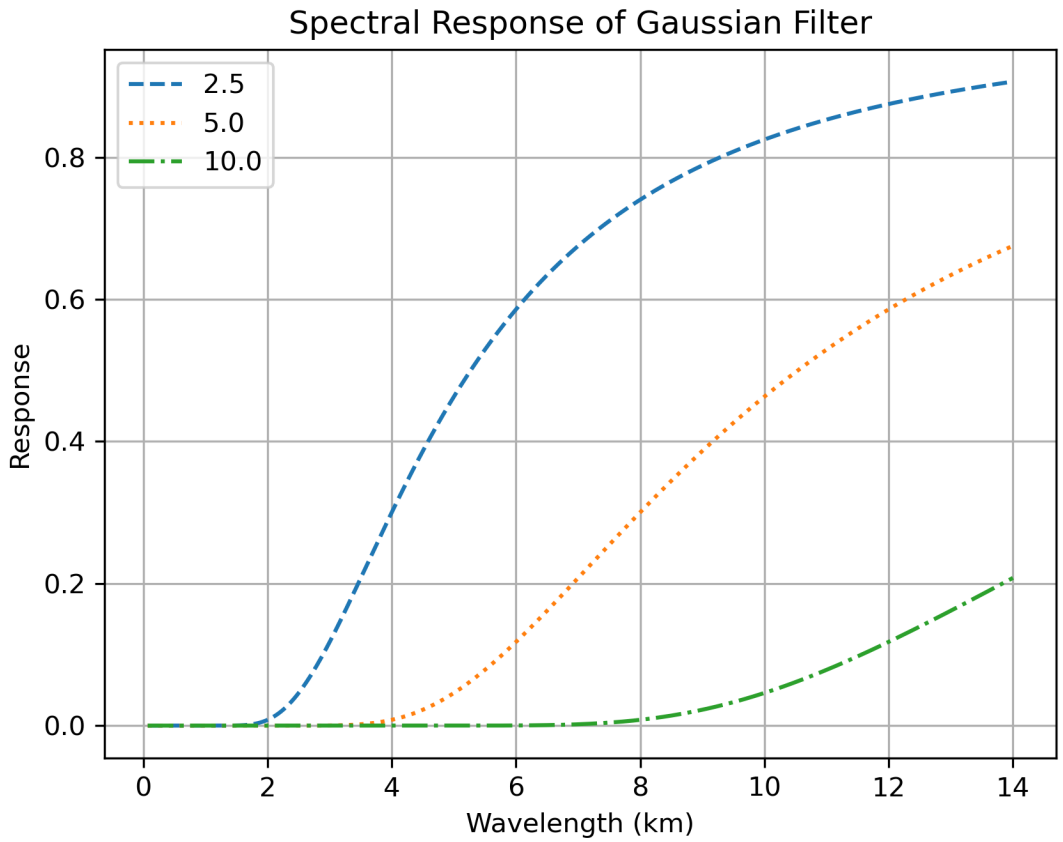

Figure 2: Normalized spectral response functions for varying Gaussian filter sigma sizes. The vertical axis is a logarithmic scale representing the size of features in the filter. The wavelength should be in km.

Optical Flow for Cloud-Top Divergence Derivations in Satellite Imagery

Once the *u*- and *v*- motion fields are computed, divergence can be derived. Analytically this is defined as

$$\nabla \cdot \mathbf{u} = \frac{\partial u}{\partial x} + \frac{\partial v}{\partial y}$$

where $\nabla = \left[\frac{\partial}{\partial x} \quad \frac{\partial}{\partial y}\right]^T$ and *u*- and *v*- are the motion fields. Numerically this is done by defining a box of eight points around a center point, (i, j), and summing the 1) Δv along the top and bottom borders and 2) Δu along the side borders. This gives the divergence at point (i, j) in pixel value, and a conversion using a latitude-longitude Haversine distance formula is used to go to kilometers.

Bilateral Filter

The Bilateral Filer (BF) was originally created for signal processing to reconstruct temporal distortions in signals caused by either the sender or during transfer. Since then, the BF was recognized to have used as an image processing technique that removes small scale brightness perturbations ("additive noise") in an image while maintaining sharp, large-scale features. It is a nonlinear operator, meaning its effect on any given pixel is different than any other pixel. Due to its nonlinearity, its effect cannot be quantified in a signal response function (SRF), but the individual filters can be. This contrasts with a strictly Gaussian image filter which creates blur along the edges of features and highlights the robustness of BFs to various types of illumination changes and motions. The general bilateral filter equation is:

$$I_{filtered}(x) = \sum_{x_i \in \Omega} I(x_i) f\big(I(x_i) - I(x)\big) g(x_i - x)$$

The spatial and brightness filters, I and g respectively, can be defined in many ways. The most common filters used for image processing are Gaussian filters (see Appendix).

While previous studies have already explored the relationship between CTD, DC intensity, and severe weather indicators, this paper aims to understand the effects of the BF on OF motion fields and subsequent CTD calculations in an attempt to attenuate unwanted CTD signals.

Defining the Case Studies

CTD with varying bilateral filter sizes were analyzed on two cases of convection. In preparation for *HWT* 2025, it was advantageous to observe CTD over the central plains of the U.S. during the mid-spring tornado season when *HWT* is typically conducted. The other case was an application of CTD in the tropics. Mesosectors in tropic latitudes are rare, a single mesosector was positioned off the Northeast coast of South America for a five-day period.

This study focuses on the development of maximum CTD and minimum IR signals withing the case study domain. The minimum IR is a proxy for both the CTC location during the growth phase of the storm and as OT location estimate during its mature phase. This approximation is subject to uncertainties, as the OT can have warmer temperatures that the surrounding anvil, but the cases were chosen to avoid this exception. Analyzing maximum CTD signals is useful for identifying thresholding values that correspond to critical features in the storm. Finally, the spatial separation between these two maxima/minima signals was analyzed. Proximity should be close

for mature phases of the storm, and a properly operating bilateral filter should account for this. Furthermore, the change in proximity with time provides a quantitative representation for the visual inconsistency, or “spiderwebbing,” of CTD signals.

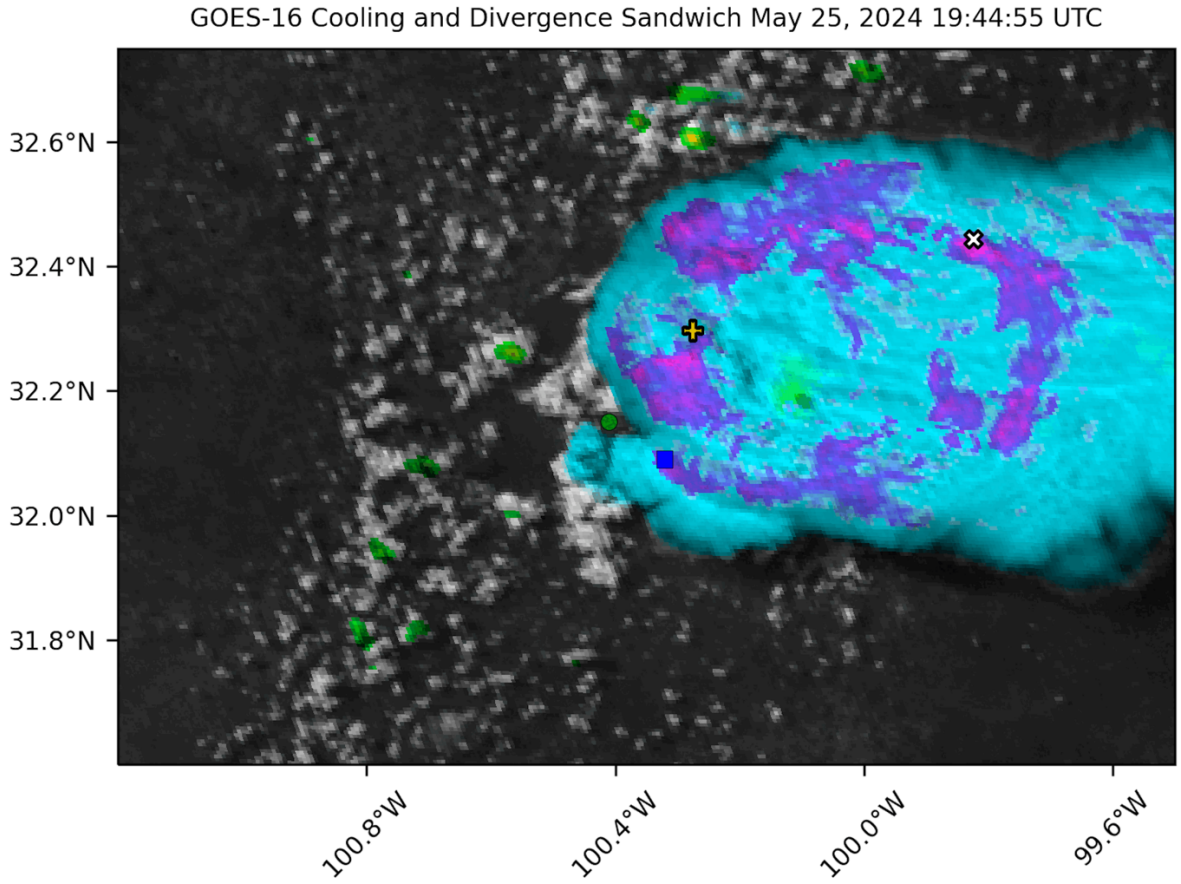

Figure 3: Example of "Spiderwebbing" in the Cloud-Top Cooling and Divergence Sandwich. The "Spiderwebs" are visible mainly on the outer edges of the anvil, but also extend inward. The same color scale is used as in Figure 4.

Section 4. Results

Case Study: May 25, 2024. Taylor County, Texas

The Taylor County, Texas case produced a supercell under strong vertical shear conditions. The area was under an enhanced to moderate SPC Day-1 Categorical Outlook. This storm is a good benchmark for CTD in relation to common severe deep convection in the Central Plains as it exhibits signs of updraft maintenance (beyond ordinary cell convection overturning) and numerous severe weather reports at the ground including large hail and strong winds..

The storm formed at 18:08 UTC with a burst of CTC, followed by the first indication of CTD at 18:19 UTC. CTD intensified until about 19:15 UTC, marked by SPC reports of hail (MRMS MESH ≥ 1.0 in) and wind (Figure 4b). Shortly after, a cirrus plum formed, and the storm updraft began to weaken (or cycle; Figure 4c). Downdrafts associated with both the rear and forward flanks began to dominate, leading to a weakening of the northern updraft (Figure 5b). This transition is reflected in the anvil formation and an SPC wind report, as the core of the storm shifts southward (Figure 5c). Once the second updraft developed, there was another wind report and an EF-1 tornado at 20:49 UTC, shown in Figure 4d.

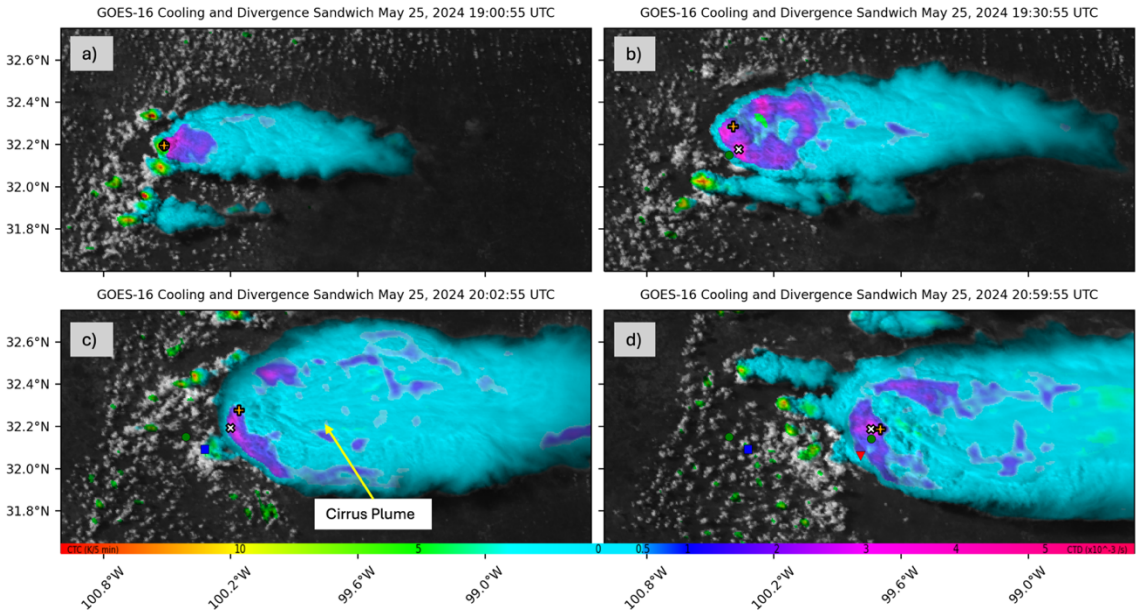

Figure 4: CTC and CTD sandwich product, which blends the visible imagery (brightness textures) with the CTC (cyan to hotter colors) and CTD (cyan to cooler colors) over the Taylor County, Texas supercell on May 25, 2024, at 1900 UTC. The orange plus shows the minimum IR and the white cross shows the maximum CTD; SPC storm reports are also displayed.

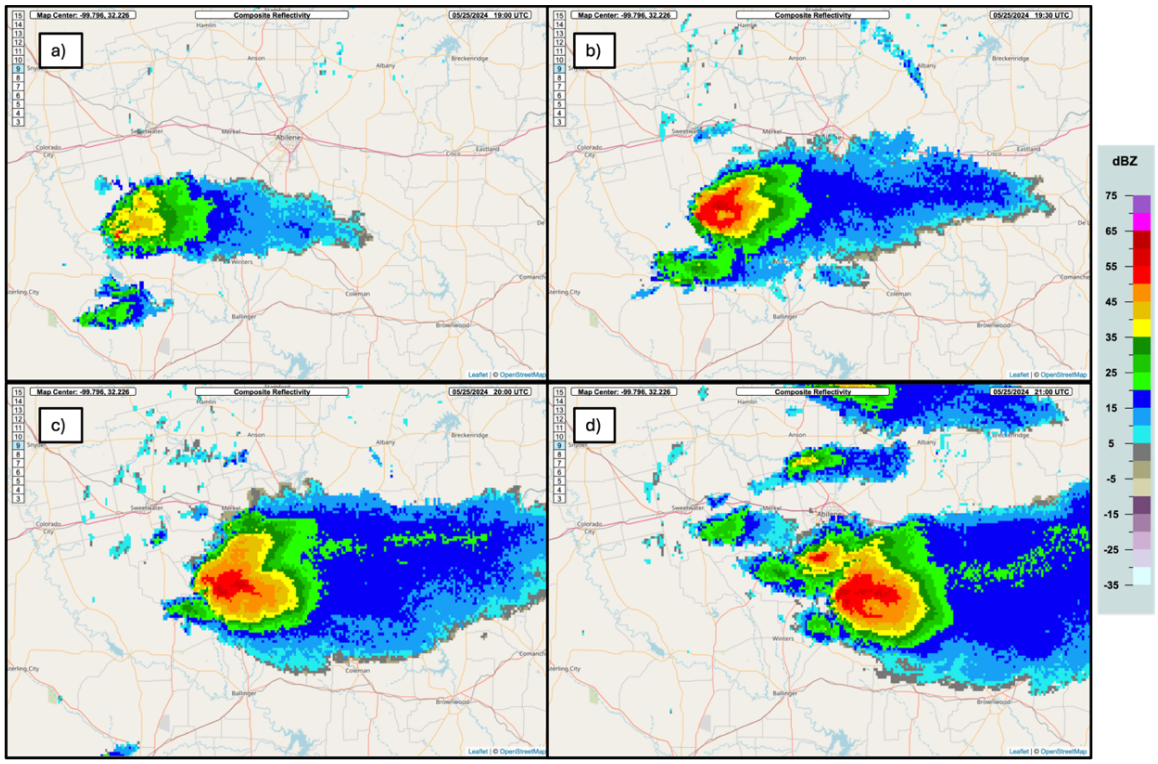

Figure 5: Composite Radar Reflectivity of Taylor County, Texas supercell from the MRMS product at the same times as Fig. 4.

Case Study Analysis: May 25, 2024. Taylor County, Texas

This supercell exhibits classic cyclic behavior that corresponds to storm intensity parameters (wind, hail, tornado-formation). CTD values for the . The initial updraft formed up to 18:18 UTC and is represented in **Error! Reference source not found.** Time series observations show the impact of using different bilateral smoothing filters on the maximum observed CTD (Fig. 7). The initial updraft exhibited strong CTC, with a minimum IR brightness temperature that drops from 280K to 228K in a period of about 35 min (average -1.49 K/min cooling rate). The updraft reached the top of the boundary layer and quickly formed an anvil, indicated by both a decrease in the CTC (-0.20 K/min) and a sharp spike in CTD across all bilateral filter sizes, shown in **Error! Reference source not found.**a-c for no filter, sigma size 2.5 and 5.0 respectively. From 18:15 UTC to 18:50 UTC marks the first mature pulse of the storm, in which the first updraft center both forms the anvil and dissipates itself. At this point, the presence of the bilateral filter is noticeable in the CTD signals, as without the filter the signal is extremely variable and indistinct from other phases of the storm (**Error! Reference source not found.**a), whereas both the filter sizes reflect

this phase with slight yet distinguishable downward trends in maximum CTD (**Error! Reference source not found.**b-c).

The second pulse forms and reaches the top of the boundary layer, initiating anvil expansion along the southern rear flank of the storm. The maximum CTD and IR minimum locations track this shift: CTD signals surge from 18:50 UTC to 19:06 UTC during the section labeled "Pulse 1" in **Error! Reference source not found.**d, and the IR undergoes another cooling phase at about -0.53 K/min: this pulse is virtually unresolvable without the bilateral filter. A brief period of decreasing CTD with continual IR cooling, followed by a quick increase in CTD that was also characterized by MRMS MESH $\geq$ 1in. and an SPC hail report (shaded turquoise and green circle in **Error! Reference source not found.**d respectively). This contrast between CTD trends before severe storm (starting at 18:49 UTC for the CTD increase to the 19:04 UTC MRMS MESH hail size greater than 1in) reports is visually easy to see with a bilateral filter size of 2.5, but overly subtle with 5.0. Regarding proximity for this first intensification phase, the maximum CTD location is very sporadic without the bilateral filter but tracks consistently with both the bilateral filter size. There is a brief jump at ~18:50 UTC for sigma size 2.5 due to a spatially small but large signal CTD far down storm.

Another spike in CTD is at 19:06 UTC which is followed by MRMS MESH hail size greater than 1in by 14min. Two SPC reports of hail and one of wind were recorded during this pulse. The third main maximum CTD increase starting at 19:20 UTC is the first indication of the second, southern updraft center dominating which is confirmed by composite reflectivity in Figure 5b. CTD undergoes a marked increase in both no bilateral filter and bilateral filter sigma size of 2.5, but is indistinguishable from the previous pulses when the filter sigma size is 5.0. During this pulse, MRMS MESH has hail greater than 1in. Again, the decrease followed by the increase in CTD acts as a strong indicator of storm intensification, but of which occurs before SPC reports. During this phase, CTD without bilateral filtering has significant "spiderwebbing;" this effect is mostly diminished with sigma size 2.5 and completely attenuated with 5.0. Nevertheless, the "spiderwebbing" effect is visually negligible with filter size 2.5, as shown in Figure 4c. The fact that CTD decreases after this pulse across all cases is because a smaller storm began to form at ~19:30 UTC and suffocated the southern updraft of the main storm at ~19:35 UTC. Also during this phase was the formation of the cirrus plume that can affect both CTD signals and IR minimum values associated with the main updraft.

The second updraft continues to mature from ~19:40 UTC to ~20:10 UTC, during which the CTD drops for both no bilateral filter and filter size 2.5. This decrease is best captured by the filter size 2.5 bilateral filter – without a filter, CTD is very sporadic, and there is almost no meaningful decrease with filter size 5.0. There is another intensification of the main updraft at ~20:12 UTC that is accompanied by large hail and ended with an SPC tornado report. All CTD signals capture this intensification, but without the filter the signal is just as noisy as the previous deintensification. The filtered CTD signals capture the intensification, but the filter size 2.5 shows a significant increase in CTD signal.

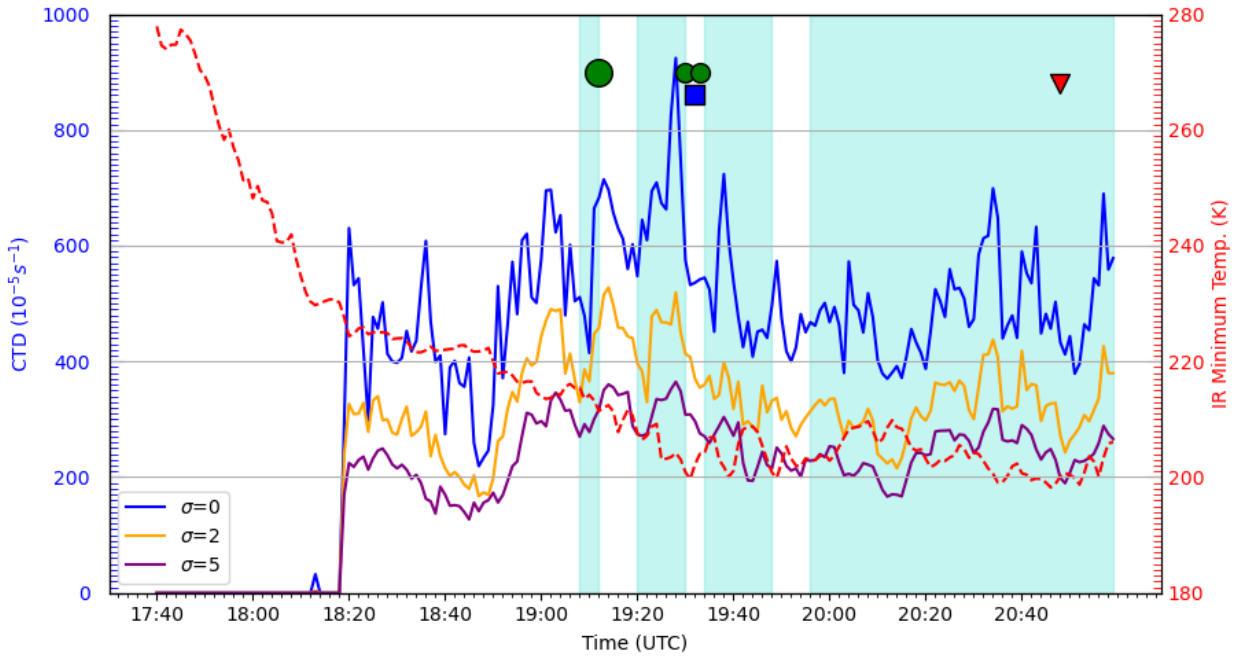

Figure 6: Maximum CTD and minimum IR (dashed red) trends and for all bilateral filter sizes (solid blue, yellow, maroon lines), with hail sizes greater than 1.0in shaded turquoise. SPC reports for hail (green circle), wind (blue square), and tornado (red triangle) are also shown.

After analysis of CTD thresholds for this case, the following values and ranges were estimated:

$$\sigma = 0.0;\ \sim 6 \pm 2 \cdot 10^{-3}\,\frac{1}{s}$$

$$\sigma = 2.5;\ \sim 4 \pm 0.5 \cdot 10^{-3}\,\frac{1}{s}$$

$$\sigma = 5.0;\ \sim 3.2 \pm 0.2 \cdot 10^{-3}\,\frac{1}{s}$$

Threshold values for CTD signals with no bilateral filter have little value in this case due to the amount of noise.

Case Study: January 15, 2020. ATOMIC Testbed Mesosector

Tropical convection was studied in the January 15, 2020, mesosector located off North-East coast of South America. From the five-day period of the location of this mesosector, this case shows the only indications of CTD related to deep convection. Unfortunately, there is no SPC report or radar data to cross-check this case.

January 15, 2020, saw temperatures around 75-80ºF and a low shear environment. Small pockets of convection were popping up constantly, and one cell began to exhibit vertical development, indicative of deeper convective (Figure 7a). Nevertheless, the convection was relatively weak. At roughly 14:45 UTC the storm produced CTD signals (Figure 7b), but significant anvil formation was minimal in the meridional directions. Instead, the storm spreads out zonally, both East and West (due to low shear), a trend which is shown in Figure 7 b-d. The storm completed a full cycle in one hour from roughly 14:30 UTC to 15:30 UTC and likely only consisted of one main updraft (consistent with ordinary cell convection) that quickly dissipated after it reached the top of the boundary layer.

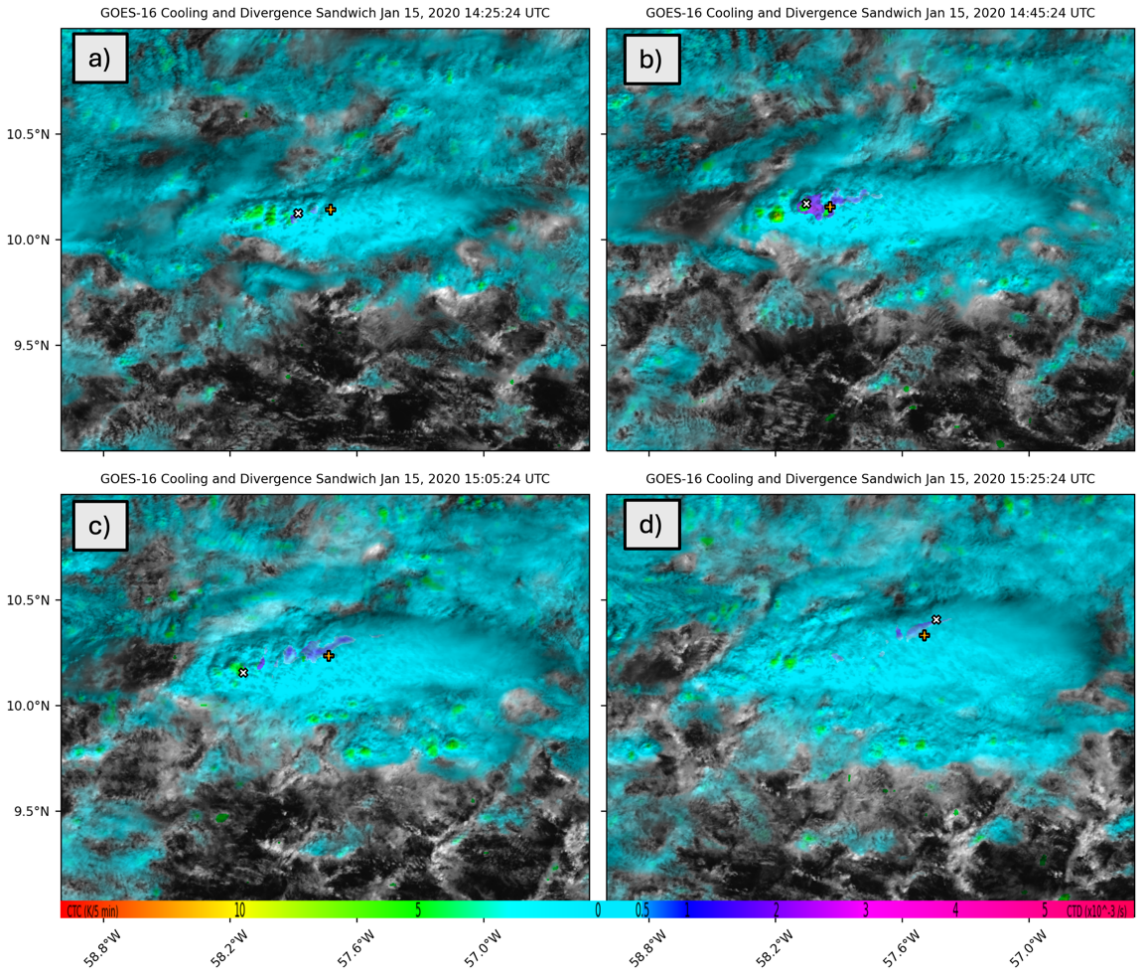

Figure 7: Same as Fig 4, now over tropical convection (chronologically from (a) to (d)) over the Atlantic Ocean northeast of South America.

The CTD threshold value ranges for this case are:

$$\sigma = 0.0;\ \sim 3 \pm 0.5 \cdot 10^{-3}\,\frac{1}{s}$$

$$\sigma = 2.5;\ \sim 2.3 \pm 0.3 \cdot 10^{-3}\,\frac{1}{s}$$

$$\sigma = 5.0;\ \sim 2.1 \pm 0.2 \cdot 10^{-3}\,\frac{1}{s}$$

These threshold ranges are not crosschecked with any severe weather reports and therefore do not hold credence.

Case Study Analysis: January 15, 2020. ATOMIC Testbed Mesosector

Tropical environments typically have weaker updrafts (given the lack of capping to allow for explosive convection in very large instability, and lack of deep layer shear to support updraft

rotation and maintenance). Hence, signals from CTD (which rely on strong $\frac{\partial w}{\partial z}$) are relatively weak compared to mid-latitude convection.

The Atlantic Tradewinds Ocean-Atmosphere Mesoscale Interaction Campaign (ATOMIC) 2020 Field Campaign located a GOES-16 mesosector over the North-East coast of South America for a five-day period. During this period, two cases of deep convection resulted in CTD signals that met the $0.5 * 10^{-3} \frac{1}{s}$, which is the threshold value used to separate signal from noise in the OCTANE CTD products. The storm in this case did not exhibit strong CTC signals – tropical storms with larger updrafts might result in larger CTC and CTD, but this was not observed.

CTD signals were associated largely with the northern flank of the storm. Both the minimum IR and maximum CTD locations were sporadic on all bilateral filter sizes. This trend is shown in Figure 8 – all bilateral filter sizes had large fluctuation in proximity. Maximum CTD did become more spatially consistent with larger bilateral filter sizes, so this phenomenon is more likely due to the sporadic location of the minimum IR.

Without the bilateral filter, CTD signals were severely "spiderwebbed" during 15:00 UTC to 15:30 UTC. Strong signals at and after 14:40 UTC do correspond to the peak in anvil formation and storm intensity (Figure 8a) and track consistently with CTC signals. With a bilateral filter sigma size of 2.5, "spiderwebbing" effects are completely removed while maintaining key features in updraft intensity, and contrast to the surrounding CTD signals (Figure 8b). Sigma size of 5.0 almost completely attenuated any meaningful CTD signals from 15:00 UTC to 15:30 UTC and did not show a better proximity relation than a sigma size of 2.5 (Figure 8c). In all bilateral filter sizes, maximum CTD has a nearly inverse relation with minimum IR and is best shown with a sigma size of 2.5 (Figure 8d). It accurately represents subtle increase in anvil formation at 15:09 UTC and during the initial convective phase from 14:12 UTC to 14:40 UTC. Nevertheless, this case study shows that even a properly filtered CTD derivation is not representative of tropical convection intensity, as there is not a meaningful vertical-horizontal mass continuity relation (i.e. components of the updraft do not immediately spread horizontally outward, but rather have a smooth transition from vertical to horizontal movement with large periods of movement that contain components of both horizontal and vertical movement which is neglected in this 2D representation of motion fields).

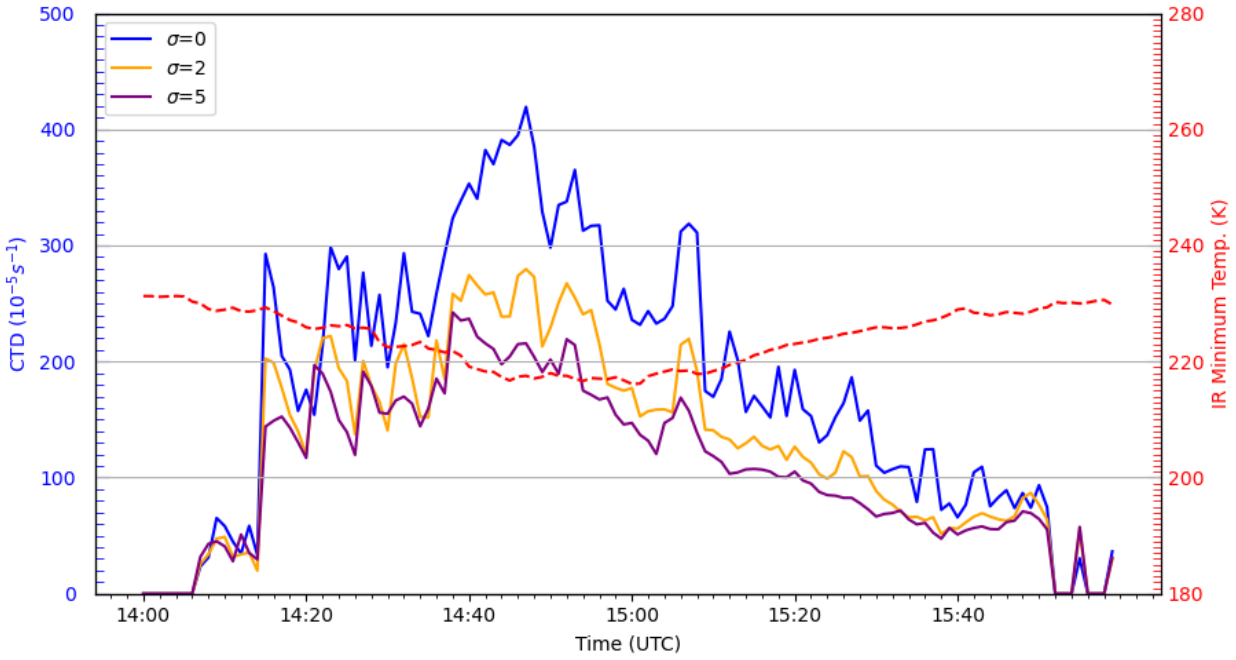

Figure 8: Maximum CTD (solid lines) and minimum IR (red dashed line) trends for all bilateral filter sizes.

Section 5. Conclusion

The application of a BF to OF motion fields effectively attenuates any sub-storm features that cause visual "spiderwebbing" in CTD signals for mid-latitude convection. For the mesoscale storms studied in this paper, it is determined that a BF sigma size of 2.5 is optimal to both preserve relevant features and remove unwanted signals. These features include 1) relative maximum CTD signal values with respect to previous storm pulses, indicative of cyclical storm formation (as opposed to sigma size 5.0, which maintained a relatively constant CTD that only fluctuated around a constant value), 2) increases in CTD roughly 15-25 min before severe weather, 3) proximity between maximum CTD and overall bulk CTD signal with the minimum IR. These findings were particularly prevalent with the Taylor County, Texas supercell in which the conversion between updraft and outward flow was strong. However, for tropical convection, CTD was less valuable. The updraft to outward flow relation is more tenuous resulting in diminished CTD signals, and higher equilibrium level means severe weather might occur before outward flow initiates.

Spatial filtering also reduced the overall maximum CTD signals. In general, a BF with sigma size of 2.5 reduced CTD signals by ~38%, while a sigma size of 5.0 led to a ~60% reduction. The cloud-top cooling and divergence sandwich product color scale must be normalized using

these percentages with respect to the BF size used, noting that larger BF sizes will result in broader spatial CTD signals not related to severe storm features.

From these reductions in magnitudes and the time-series for each case study, CTD severe weather threshold value ranges were determine (for the Texas case) to be $4 \pm 0.5 \cdot 10^{-3} \frac{1}{s}$ for sigma size 2.5, and $3.2 \pm 0.2 \cdot 10^{-3} \frac{1}{s}$ for sigma size 5.0. Both these ranges allowed for a 15-25min lead time from when the CTD threshold was met to severe weather indications from MRMS MESH and SPC reports.

While this study successfully shows the significance of a spatial filter in CTD derivations, it is subject to multiple limitations. The first is the lack of crosscheck data for the tropical storm case study; While the CTD was weaker, there were no reports to confirm if the observed storm was severe. Second is the use of the minimum IR proximity with maximum CTD. Warm cirrus plumes can mask minimum IR temperatures at the top of the anvil, which in turn mask the true location DC. Therefor the "proximity" parameter lacks meaning once the minimum IR value ceases tracking DC. Nevertheless, proximity adds value to this study in that it quantifies the visual "spiderwebbing" of CTD signals. Another limitation is in the finite-element differencing method used to compute divergence, *du/dx* and *dv/dy*, due to the assumption of strictly 2-dimensional updraft physics – an assumption that neglects vertical motions. This can be extended to the full profile of the atmosphere: CTD is a measure of the top 2-dimensional field, whereas updraft characteristics vary with altitudes and create 3-dimensional flow fields. The last main limitation is the number of case studies. Analysis of a wider range of both sizes and locations of storms with an added number of BF sizes would illuminate a more robust/quantitative relationship between BF size, CTD magnitude, and storm characteristics.

Section 6. Appendix

The Bilateral Filter

The general definition of the BF in image processing is:

$$I_{filtered}(x) = \sum_{x_i \in \Omega} I(x_i) f\big(I(x_i) - I(x)\big) g(x_i - x)$$

where $I_{filtered}(x)$ is the output filtered image, and $I(x_i)$ is the original input image. The summation represents all the elements, x_i, within a Gaussian Kernel, Ω. f and g are the spatial and

intensity weighting functions within the Gaussian Kernel respectively, which are both themselves gaussian distributions. The spatial-weighting function biases pixels that are closer to the point x_i, while the intensity-weighting function biases pixels that have intensity like that of x_i. A visualization of the BF is shown in Figure 9.

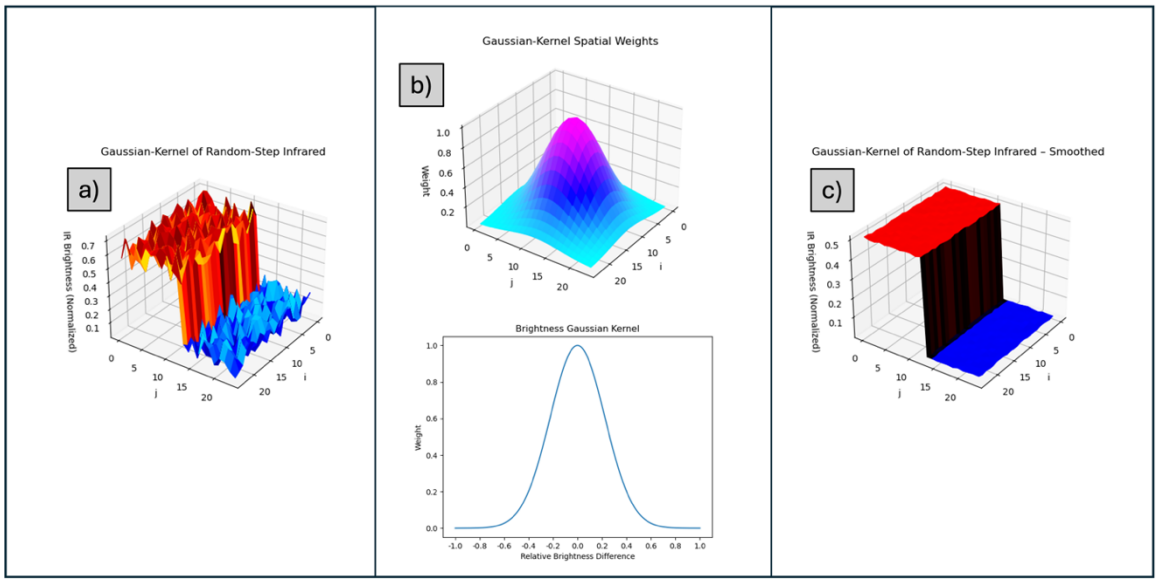

Figure 9. A Bilateral Filter visualization showing (a) a piece-wise step-function subject to additive noise, (b) the Gaussian spatial weighting kernel (on top) and the Gaussian brightness kernel (on bottom), and (c) the resultant filtered step-function.

The spatial Gaussian kernel used is defined as:

$$g(x_i - x) = \left(\frac{1}{\pi\sigma^2}\right) e^{-r^2/2\sigma^2}$$

Here, $g(x_i - x)$ was applied to the u- and v- motion-fields separately using channel 02 0.64µm VIS imagery, denoted as g_u and g_v. Each g_u and g_v were calculated, then used to normalize the weighting in the overall kernel, Ω.

The brightness Gaussian kernel is:

$$f\big(I(x_i) - I(x)\big) = e^{-\frac{\left(I(x_i) - I(x)\right)^2}{\epsilon^2}}$$

Where ϵ is 20 pixels. The kernel size is the integer truncation of $(1.5 \cdot \sigma)$, in which 1.5 was the factor that quasi-optimized the compute time with weighting of point x_i. $I(x_i)$ and $I(x)$ are the 10.3µm IR brightness temperatures.

Optical Flow Techniques

The Brox method constructs a minimizable *global energy functional* consisting of a "data term" and a "prior term":

$$E_{Global} = E_{Data} + \lambda E_{Prior}$$

The *brightness constancy* and *brightness gradient constancy constraint* defines E_{Data}orms the famous *optical flow constraint equation:*

$$I_x u + I_y v + I_t = 0$$

The assumption that pixel illumination is constant can result in errors, so the *gradient constancy constraint* can also be applied:

$$\nabla I(x, y, t) = \nabla I(x + u, y + v, t + 1)$$

So far, these provide one constraint for the two unknowns of the *motion field*. The E_{Prior} favors certain flow fields over others and can be defined in many ways. The Brox method uses the L1 norm – a robust penalty function. From this, E_{Global} can be minimized in several ways, but the Brox method uses *sparse-to-dense matching methods* (Brox et al. 2009) that can estimate even large feature displacements. The Brox method poses itself as a set of nonlinear Euler-Lagrange equations which are solved with numerical methods, such as Gauss-Seidel (Brox et al. 2009).

Section 7. References

Apke, J. M., and J. R. Mecikalski, 2021: On the Origin of Rotation Derived from Super Rapid Scan Satellite Imagery at the Cloud-Tops of Severe Deep Convection. *Monthly Weather Review*, https://doi.org/10.1175/MWR-D-20-0209.1.

——, ——, K. Bedka, E. W. McCaul, C. R. Homeyer, and C. P. Jewett, 2018: Relationships between Deep Convection Updraft Characteristics and Satellite-Based Super Rapid Scan Mesoscale Atmospheric Motion Vector–Derived Flow. *Monthly Weather Review*, **146**, 3461–3480, https://doi.org/10.1175/MWR-D-18-0119.1.

——, Y.-J. Noh, and K. Bedka, 2022: Comparison of Optical Flow Derivation Techniques for Retrieving Tropospheric Winds from Satellite Image Sequences. *Journal of Atmospheric and Oceanic Technology*, **39**, 2005–2021, https://doi.org/10.1175/JTECH-D-22-0057.1.

——, Hilburn, K. A., Miller, S. D., and Peterson, D. A., 2020: Towards objective identification and tracking of convective outflow boundaries in next-generation geostationary satellite imagery, Atmos. Meas. Tech., 13, 1593–1608, https://doi.org/10.5194/amt-13-1593-2020.

455 ——, Tobin, J., Noh, Y. J., White, C., Haynes, J., 2024: Using Optical Flow Temporal
456 Interpolation of Satellite Imagery to Assist Multi-Sensor Global Cloud Product
457 Composites. *Journal of Atmospheric and Oceanic Technology*.

458 Baker, S., D. Scharstein, J. P. Lewis, S. Roth, M. J. Black, and R. Szeliski, 2011: A Database and
459 Evaluation Methodology for Optical Flow. *Int J Comput Vis*, **92**, 1–31,
460 https://doi.org/10.1007/s11263-010-0390-2.

461 Brox, T., Bruhn, A., Papenberg, N., Weickert, J., 2004: High Accuracy Optical Flow Estimation
462 Based on a Theory for Warping. *European Conference on Computer Vision*, **4,** 25-36,
463 http://dx.doi.org/10.1007/978-3-540-24673-2_3.

464 Elad, M., 2002: On the origin of the bilateral filter and ways to improve it. *IEEE Trans. on*
465 *Image Process.*, **11**, 1141–1151, https://doi.org/10.1109/TIP.2002.801126.

466 Fortun, D., P. Bouthemy, and C. Kervrann, 2015: Optical flow modeling and computation: A
467 survey. *Computer Vision and Image Understanding*, **134**, 1–21,
468 https://doi.org/10.1016/j.cviu.2015.02.008.

469 Horn, B. K. P., and B. G. Schunck, 1981: Determining optical flow. *Artificial Intelligence*, **17**,
470 185–203, https://doi.org/10.1016/0004-3702(81)90024-2.

471 Mecikalski, J. R., T. N. Sandmæl, E. M. Murillo, C. R. Homeyer, K. M. Bedka, J. M. Apke, and
472 C. P. Jewett, 2021: Random Forest Model to Assess Predictor Importance and Nowcast
473 Severe Storms using High-Resolution Radar–GOES Satellite–Lightning Observations.
474 *Monthly Weather Review*, https://doi.org/10.1175/MWR-D-19-0274.1.

475 Rogers, M. A., Apke, J. M., Longmore, S. P., 2020: Meso-anywhere sectors from GOES-R -
476 optical flow techniques for global 1-minute imagery. *American Geophysical Union*,
477 2020AGUFMA008.0018R.

478 Schmit, T. J., and Coauthors, 2013: Geostationary Operational Environmental Satellite (GOES)-
479 14 super rapid scan operations to prepare for GOES-R. J. Appl. Remote Sens.,7, 073462,
480 https://doi.org/10.1117/1.JRS.7.073462.

481 Schultz, C. J., W. A. Petersen, and L. D. Carey, 2009: Preliminary development and evaluation
482 of lightning jump algorithms for the real-time detection of severe weather. *J. Appl.*
483 *Meteor. Climatol.*, 48, 2543–2563, https://doi.org/10.1175/2009JAMC2237.1.

484 ——, ——, and ——, 2011: Lightning and severe weather: A comparison between total and
485 cloud-to-ground lightning trends. *Wea. Forecasting*, **26**, 744–755,
486 https://doi.org/10.1175/WAF-D-10-05026.1.

487 Thiel, K., 2024: GOES-R and JPSS Proving Ground Demonstration at the Hazardous Weather
488 Testbed 2024 Spring Experiment. *NOAA Hazardous Weather Testbed (HWT).*

489 U.S. Billion-dollar Weather and Climate Disasters, 1980 - present (NCEI Accession 0209268),
490 2025. *Billion-Dollar Weather and Climate Disasters*. Accessed 11 April 2025,
491 https://www.ncei.noaa.gov/access/metadata/landing-
492 page/bin/iso?id=gov.noaa.nodc:0209268.

493 Velden, C., and Coauthors, 2005: Recent Innovations in Deriving Tropospheric Winds from
494 Meteorological Satellites. *Bulletin of the American Meteorological Society*, **86**, 205–224,
495 https://doi.org/10.1175/BAMS-86-2-205.

496 Zhang, J., and Coauthors, 2016: Multi-Radar Multi-Sensor (MRMS) Quantitative Precipitation
497 Estimation: Initial Operating Capabilities. *Bulletin of the American Meteorological*
498 *Society*, **97**, 621–638, https://doi.org/10.1175/BAMS-D-14-00174.1.

499 Zimmer, H., A. Bruhn, and J. Weickert, 2011: Optic Flow in Harmony. *Int J Comput Vis*, **93**,
500 368–388, https://doi.org/10.1007/s11263-011-0422-6.
501